ELSEVIER

Materials Science and Engineering A260 (1999) 108–123

MATERIALS SCIENCE & ENGINEERING A

Microstructure and mechanical properties of two-phase $Cr-Cr_2Nb$, $Cr-Cr_2Zr$ and $Cr-Cr_2(Nb,Zr)$ alloys

T. Takasugi *, K.S. Kumar [1], C.T. Liu, E.H. Lee

Metals and Ceramics Division, Oak Ridge National Laboratory, Oak Ridge, TN 37831-6115, USA

Received 15 June 1998; received in revised form 9 September 1998

Abstract

The microstructures and mechanical properties of binary and ternary Cr-based alloys containing Nb, Zr, or both Nb and Zr, have been studied in both the as-cast and annealed conditions. The level of alloying in each instance was targeted to lie below, or approximately at, the maximum solubility in chromium. The as-cast microstructures of these alloys consisted of Cr-rich solid solution surrounded by small amounts of interdendritic $Cr-Cr_2X$ eutectic structure. Annealing at 1473 K resulted in solid-state precipitation of the Cr_2X Laves phase in the Cr–Nb and Cr–Nb–Zr alloys, but not in the Cr–Zr alloys. The binary Cr_2Nb phase consisted of an extensively twinned ($\{111\} < 112 >$ twins) C15 structure whereas the presence of Zr modifies its appearance substantially; the twinned C15 structure persists. Oxides were occasionally present and their compositions were qualitatively determined. Vickers hardness primarily depended upon the volume fraction of the Cr_2X Laves phase present. Age hardening due to solid-state precipitation of Cr_2X Laves phase within the Cr-rich matrix was observed in the Nb-containing alloys. The room temperature bend strength of the alloys was strongly affected by the presence of grain-boundary Cr_2X phase. It is considered that porosity as well as oxides in the alloys also lowers their bend strength. © 1999 Elsevier Science S.A. All rights reserved.

Keywords: $Cr-Cr_2Nb$ alloy; $Cr-Cr_2Zr$ alloy; $Cr-Cr_2(Nb,Zr)$ alloy; Microstructure; Mechanical properties; Laves phase; Alloy design

1. Introduction

Chromium forms the Cr_2X Laves phase (where X = Ta, Hf, Nb, Zr and Ti) as an intermediate phase in the respective Cr–X binary alloy systems, making it possible to produce two-phase microstructures in the Cr-rich regions [1]. Since the Cr_2X Laves phase generally has a high melting point, relatively low density, and high temperature strength, two-phase $Cr-Cr_2X$ alloys are of technological interest in the field of high-temperature structural materials. Two-phase microstructures of the type $Cr-Cr_2X$ are typically formed by eutectic reactions in these systems [1]. With decrease in temperature below the eutectic temperature, the solubility of the refractory element in Cr solid solution and the solubility of Cr in the Cr_2X phase can both decrease; this will result in the solid-state precipitation of Cr_2X from the Cr-solid solution, and Cr solid solution particles from the Cr_2X phase. Some work has been previously performed on microstructure and mechanical properties of two-phase $Cr-Cr_2Nb$ [2–9], $Cr-Cr_2Hf$ [10–12], and $Cr-Cr_2Ti$ [13–16] alloys. However, the results obtained so far have been below desirable levels in terms of low-temperature fracture toughness although excellent high temperature strength [2,8], and considerable room temperature compressive ductility [2,11], have been obtained. Therefore, a major issue in alloy design of two-phase $Cr-Cr_2X$ alloys is to understand and improve the deformation and fracture resistance of the Cr-rich phase. It is expected that this can be achieved by selection of solutes (such as solubility limit) and precipitation of the Cr_2X Laves phase in the primary Cr solid solution.

The selection of Cr–Nb and Cr–Zr alloys in this study is based on the consideration that there is a large difference in the solubility limit, atomic size, and chemical activity of Nb and Zr solutes in Cr-rich phase, as indicated by the two binary phase diagrams Fig. 1(a)

* Corresponding author. Present address: Institute for Materials Research, Tohuko University, Aoba-ku, Katahira 2-1-1, Sendai 980-8577, Japan..

[1] Present address: Division of Engineering, Brown University, Providence, RI 02912, USA.

0921-5093/99/$ - see front matter © 1999 Elsevier Science S.A. All rights reserved.
PII: S0921-5093(98)00981-2

and (b). For instance, the Cr solid solution range in the Cr–Nb alloy system is large (i.e. ≈ 6 at.% Nb), while that in the Cr–Zr alloy system is small (i.e. ≈ 0.6 at.% Zr). Also, the solvii of the Cr-rich phase and the Cr_2X phase in the Cr–Nb alloy system decrease rapidly with decreasing temperature, while those in the Cr–Zr alloy system remain constant or slightly decrease with decreasing temperature. Thus, these differences in phase relationship may result in different microstructures and mechanical properties. The Cr–(Nb,Zr) ternary alloys were prepared to modify the solubility of solutes and the morphology of Cr_2X precipitates in the Cr-rich phase. To study mechanical properties of the Cr matrix, all the alloys were prepared with compositions close to the solubility limit of Zr and Nb according to the two binary alloy systems. The alloys prepared were also annealed at 1473 K to alter their microstructures. The microstructures and mechanical properties of these alloys were evaluated at room temperature. The goal of this study is to understand metallurgical factors controlling the fracture resistance of the Cr-rich phase via the control of Nb and Zr solutes in the phase.

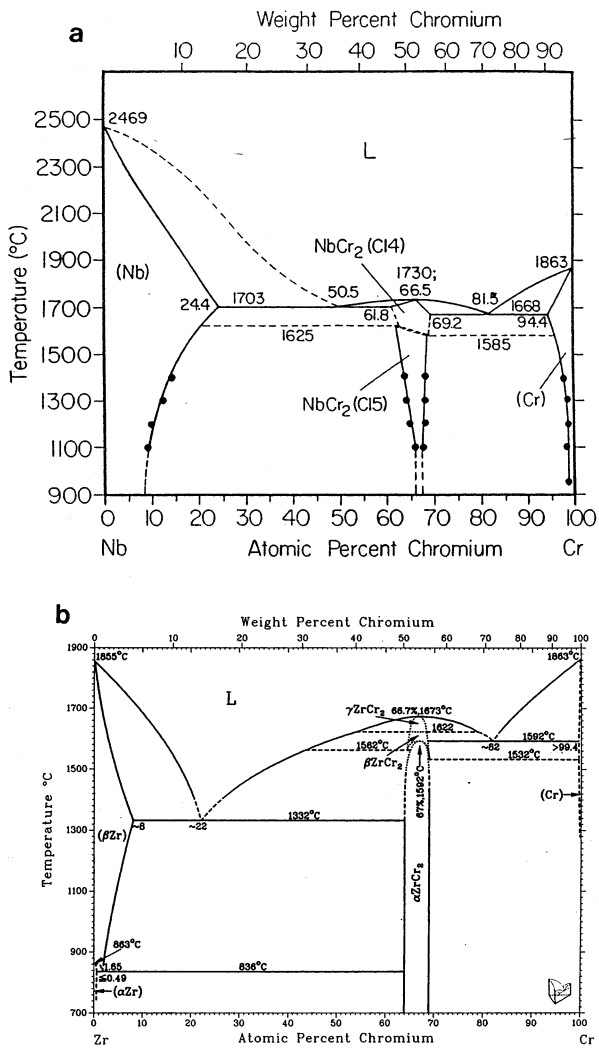

Fig. 1. (a) The binary Cr–Nb phase diagram [5], and (b) binary Cr–Zr phase diagram [1].

2. Experimental procedure

Alloys based on Cr–Cr_2X compositions were prepared by arc melting appropriate elemental constituents and drop casting into a 12.5 mm diameter and 50 mm length copper mould. Two alloy compositions were prepared in each of the two binary systems, Cr–Cr_2Nb and Cr–Cr_2Zr; one corresponds to almost the maximum solubility in the Cr-rich phase (Cr–6 at.% Nb; Cr–1 at.% Zr), and the other corresponds to half (or less) of the maximum solubility (Cr–3 at.% Nb; Cr–0.3 at.% Zr). In the Cr–Cr_2(Nb,Zr) ternary alloys, 1 at.% of Zr was substituted for Nb (Cr–5Nb–1Zr; Cr–2Nb–1Zr). To compensate for Cr evaporation during melting, excess Cr was added. Samples for microstructural examination and mechanical property measurement were sectioned from the ingots by electrodischarge machining (EDM), and then heat treated at 1473 K for 5, 20 or 100 h in vacuum ($\approx 10^{-4}$ Pa).

The as-cast and annealed alloys were first examined by optical microscopy (OM) to understand microstructural evolution during annealing. Metallographic specimens were mechanically polished and then etched in a solution of 15 g KOH, 15 g $K_3Fe(CN)_6$, and 90 ml H_2O for 5–20 s at 368 K. Electron microprobe analysis using wavelength-dispersive spectroscopy (WDS) was performed on as-cast alloys and 100 h-annealed alloys to investigate microstructure and compositions in the constituent phases. Chemical composition data for the constituent phases were collected from more than 20 locations and then averaged. Also, two-dimensional element mapping was performed. Both as-cast and 100 h-annealed samples were examined in a transmission electron microscope (TEM). Specimens used for TEM observations were cut into 3 mm disks by EDM and mechanically abraded to a thickness of ≈ 0.1 mm or less. The abraded specimens were jet-polished in a solution of 10% perchloric acid and 90% methanol at 233 K. In cases where an adequate electron-transparent area was not obtained, foils were further ion-milled for a brief time. These specimens were examined using a CM12 microscope at an accelerating voltage of 120 kV.

Room temperature Vickers hardness was measured with three different levels of load on metallographic samples. A 50 g load was used for hardness measurement in the Cr-rich phase surrounded by the eutectic Cr/Cr_2X structure. In this case, the indentation size was small enough to be located inside the primary Cr-rich phase. A 500 g load was used when an overall hardness (i.e. hardness of the alloy) covering the entire two-phase region (consisting of the Cr-rich phase and the eutectic

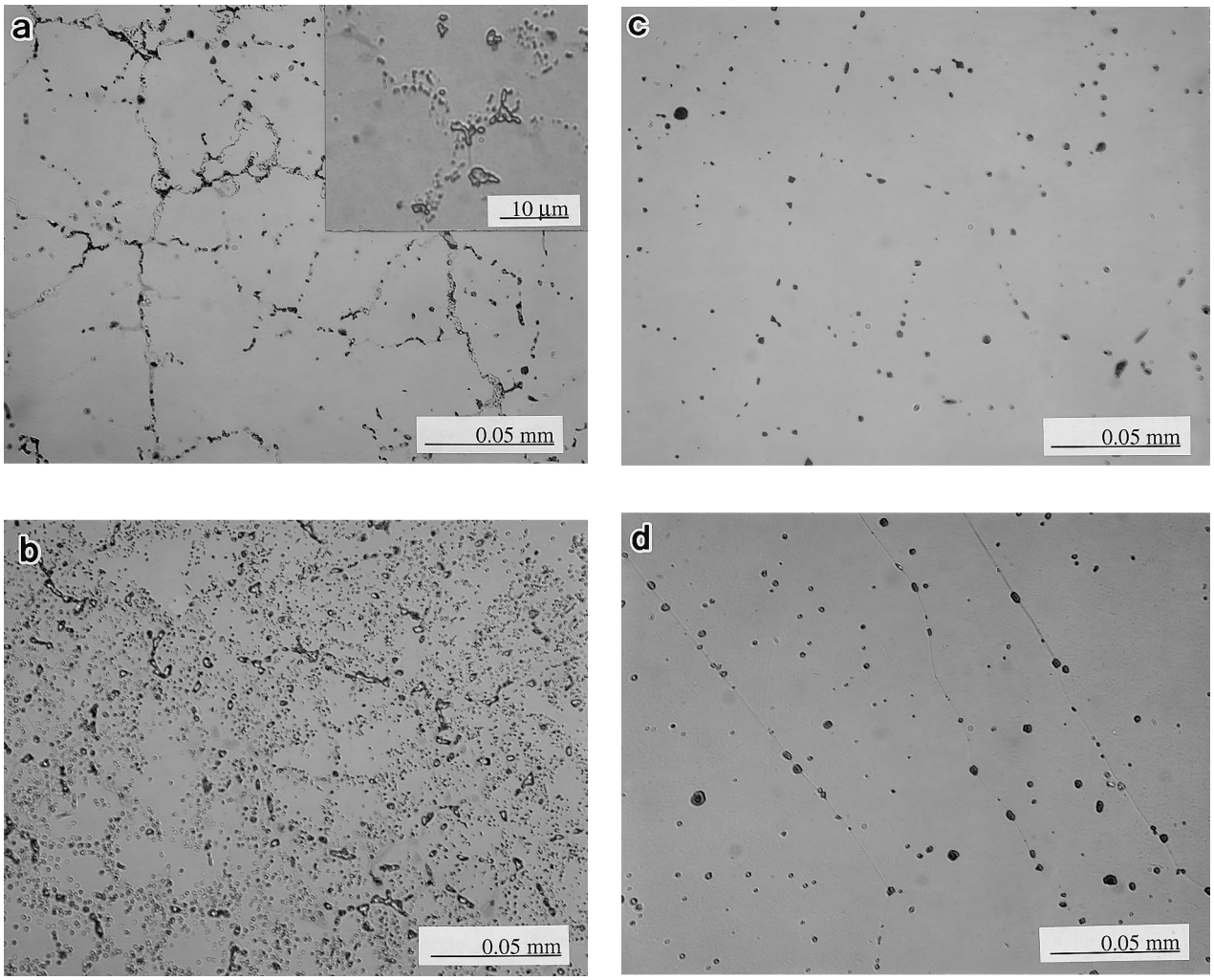

Fig. 2. Optical microstructures of the Cr–3Nb alloy (a,b), the Cr–0.3Zr alloy (c,d) and the Cr–2Nb–1Zr alloy (e,f) which were as-cast (a,c,e), and annealed at 1473 K for 100 h (b,d,f), respectively.

Cr/Cr_2X structure) was measured. In both measurements, more than 15 points were measured in order to obtain reliable values.

Rectangular specimens with dimensions of $\approx 2.5 \times 4.5 \times 20$ mm^3 were used for room temperature three-point bending tests. All specimen surfaces were mechanically abraded with up to 600-grit SiC paper. Bending tests were conducted on both as-cast and annealed alloys at a displacement rate of 0.6 mm min^{-1}. A fully articulated three-point bending fixture (with a span of 10 mm and a pushing rod of 3 mm diameter) was used for fracture of the bend specimen. The bend strength, σ_f, was calculated from a load versus displacement curve, using the relationship of $\sigma_f = 1.5Pl/wt^2$ where P is the load, l is the span (i.e. 10 mm), and w and t are the width and the thickness of the specimen, respectively. At least two specimens were used for measurement of each material condition.

3. Results

3.1. Microstructure

The microstructures of all the alloys prepared were examined metallographically. Some of them are shown in Fig. 2. The Cr–3Nb alloy in the as-cast condition shows a primary Cr-rich solid solution dendrites surrounded by a more or less continuous thin layer of Cr/Cr_2Nb eutectic structure in the interdendritic regions Fig. 2(a). According to the equilibrium phase diagram shown in Fig. 1a, this alloy composition lies below the maximum solubility of Nb in the Cr-rich solid solution and should not participate in the eutectic reaction. The presence of the eutectic structure is attributed to non-equilibrium freezing, with only limited diffusion in the solid, leading to coring and false eutectic freezing. The Cr–6Nb alloy, which is located in the composition range around (or slightly beyond) the maximum

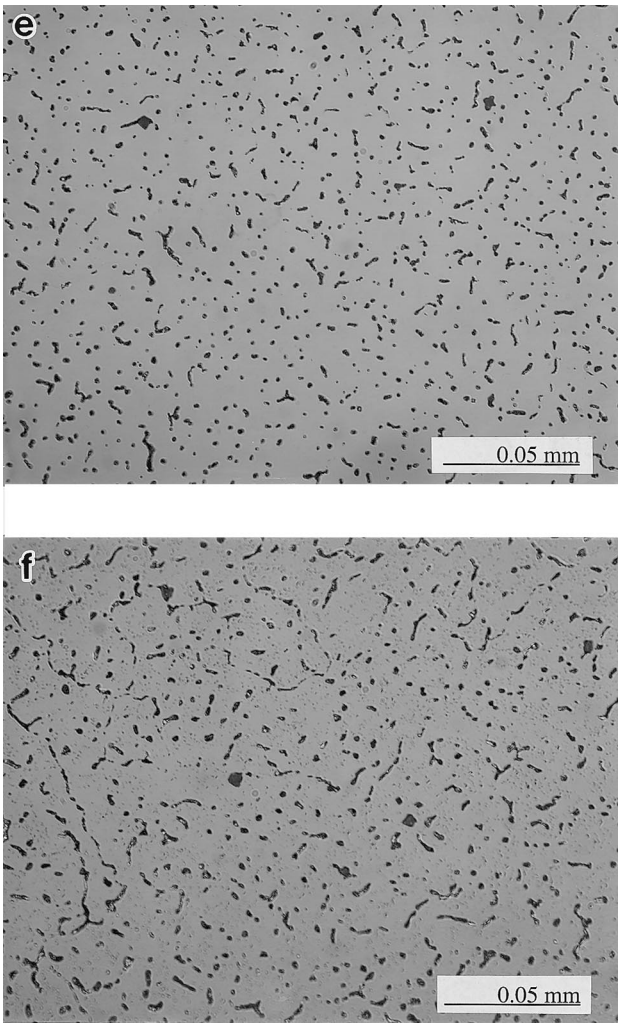

Fig. 2. (*Continued*)

showed a higher volume fraction of the Cr/Cr_2Nb eutectic structure than the Cr–3Nb allsolubility limit of Nb in the Cr-rich solid solution, oy. No precipitate was present within the primary Cr solid solution phase of both Cr–Nb alloys (at an optical microscopic resolution level) although they would be expected to occur from the decreasing solubility of Nb in the Cr-rich solid solution with decreasing temperature. This result indicates that the solid state precipitation of Cr_2Nb is sluggish and also the cooling rate in the solid state is rapid as would be expected in a copper mould. The Cr–0.3Zr alloy shows a primary Cr-rich solid solution and minor amounts of Cr_2Zr precipitates in the interdendritic regions Fig. 2(c). No Cr_2Zr precipitates could be resolved within the primary Cr solid solution dendrites. The interdendritic Cr_2Zr is thought to be a consequence of false eutectic freezing and the isolated Cr_2Zr particles are likely to be a manifestation of a divorced eutectic morphology. The microstructure of the Cr–1Zr alloy was substantially similar to that of the Cr–0.3Zr alloy except for a higher density of Cr_2Zr particles in the interdendritic locations. Thus, the low solubility of Zr in the Cr-rich solid solution is confirmed from the present observation. The Cr–5Nb–1Zr alloy showed microstructural features similar to that observed in the Cr–6Nb alloy; the primary Cr-rich solid solution was surrounded by an interconnected Cr/Cr_2X eutectic structure. The Cr–2Nb–1Zr alloy showed a microstructure somewhat different from the two binary Cr–Nb alloys and the ternary Cr–5Nb–1Zr alloy, as shown in Fig. 2(e). The dendritic structure appears more refined compared to the binary Cr–3Nb alloy (Fig. 2a), and the typical interdendritic eutectic structure if present, is not readily resolved. Rather, ligaments of what is believed to be single-phase Cr_2X, are present in these interdendritic locations. No Cr_2X precipitates were present within Cr-rich solid solution phases in both Cr–Nb–Zr ternary alloys.

The supersaturated Cr-rich solid solution precipitates out fine Cr_2Nb particles during annealing at 1473 K, and their average size increases with increasing time. For instance, Fig. 2(b) shows the microstructure of the Cr–3Nb alloy annealed at 1473 K for 100 h. An

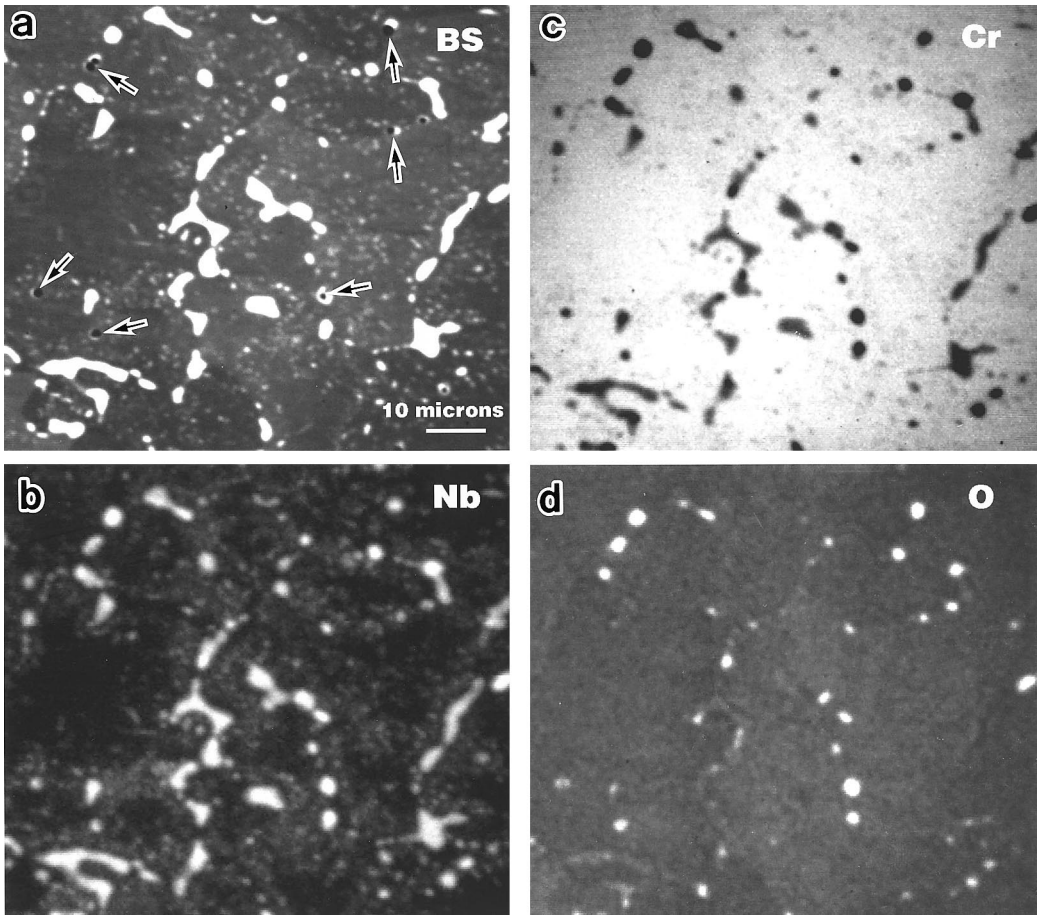

Fig. 3. (a) Backscattered electron image and two-dimensional maps of elements (b) Nb, (c) Cr and (d) O for the Cr–3Nb alloy annealed at 1473 K for 100 h.

examination of the microstructure shows a gradient in the distribution of the Cr_2Nb precipitates within the Cr-rich dendrite; there exists a precipitate-free region in the centre of each dendrite. This gradient may be attributed to an inhomogeneous distribution of Nb solute atoms from the centre of the dendrite to the interdendritic region as a consequence of non-equilibrium solidification. Similar coring effects were observed in the Cr-rich dendrites of the Cr–6Nb alloy. However, in this alloy composition, Cr_2Nb precipitates were observed to occur even in the centre of the dendrites. On the other hand, microstructural changes due to annealing were minimal for the two Cr–Zr binary alloys (at least at an optical microscopic level), as shown in Fig. 2(d). This observation is consistent with a very low solubility of Zr in the Cr-rich solid solution, as suggested by the binary phase diagram (Fig. 1b). The annealed microstructure of the Cr–5Nb–1Zr alloy is similar to that of the Cr–6Nb alloy; i.e. extensive precipitation of Cr_2X particles was observed and a precipitate-free zone (PFZ) was formed adjacent to the eutectic Cr/Cr_2X. The annealed Cr–2Nb–1Zr alloy

Table 1
Compositions of the constituent phases in the Cr–3Nb and Cr–2Nb–1Zr alloys analysed by WDS

Alloy	Heat treatment	Phase	Cr (at.%)	Nb (at.%)	Zr (at.%)
Cr–3Nb	As-cast	Laves phase	70.0	30.0	–
		Cr phase	98.1	1.9	–
	1473 K/100 h	Laves phase	63.9	36.1	–
		Cr phase	98.9	1.1	–
Cr–2Nb–1Zr	As-cast	Laves phase	75.3	13.9	10.8
		Cr phase	98.1	1.8	0.07
	1473 K/100 h	Laves phase	71.3	20.6	8.1
		Cr phase	99.1	0.9	0.02

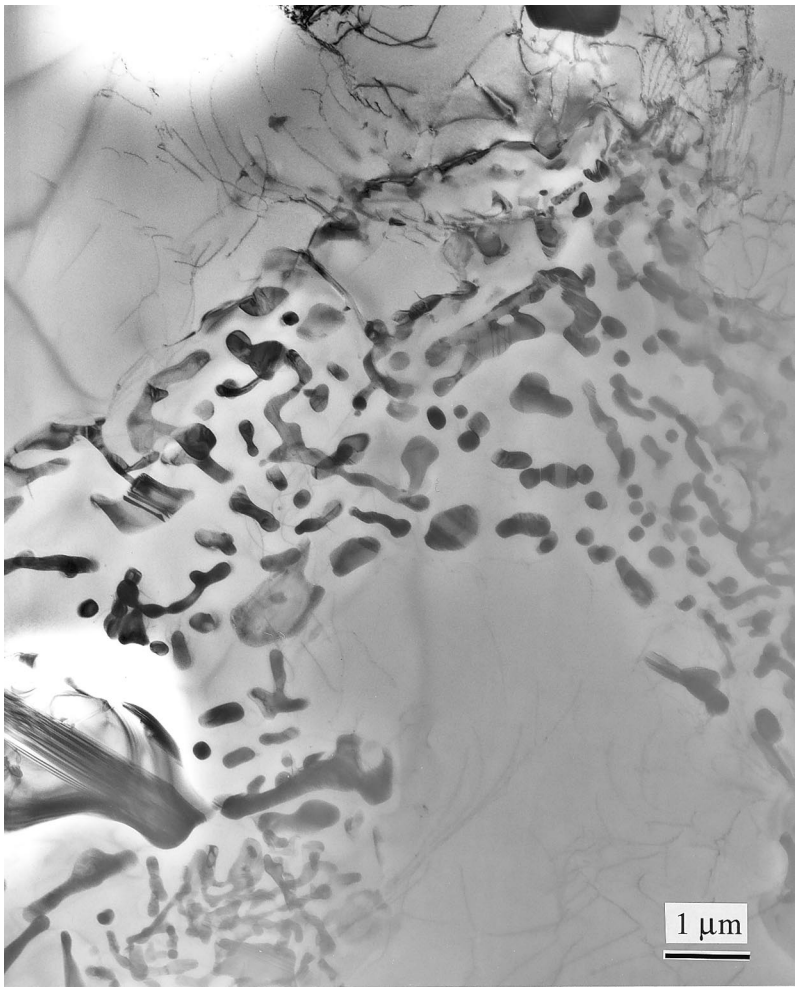

Fig. 4. TEM bright field image of the as-cast Cr–3Nb alloy.

showed a relatively homogeneous distribution of the Cr_2X precipitates within the Cr-dendrites (Fig. 2f), unlike the binary Cr–3Nb alloy where a central precipitate-free region was observed.

To investigate the microstructure and composition of alloy phases, electron microprobe analyses were performed on the Cr–3Nb alloy and the Cr–2Nb–1Zr alloy. Fig. 3 shows a backscattered electron image and two-dimensional mappings of the elements Nb, Cr and O for the Cr–3Nb alloy annealed at 1473 K for 100 h. The backscattered electron image is consistent with the annealed microstructure shown in Fig. 2(b). The composition of the constituent phases determined by WDS are summarised in art. Here, the analyses of the eutectic Cr_2Nb (or Cr_2X) precipitates were performed on relatively large particles. In the as-cast condition of the Cr–3Nb alloy, the Cr-rich dendrites contained 1.9 at.% Nb, while the eutectic Cr_2Nb contained 30.0 at.% Nb. Following annealing at 1473 K for 100 h, the Nb concentration in the Cr-rich matrix reduced to 1.1 at.% Nb. Correspondingly, the Nb concentration in the Cr_2Nb eutectic microconstituent increased to 36.1 at.% Nb. The Nb concentration in the Cr-rich matrix phase in the annealed material shown in Table 1, is probably higher than the actual values because of the existence of fine and dense Cr_2Nb precipitates that resulted from the solid state reaction during annealing. Oxide dispersions were occasionally observed, with Nb as the major constituent element. By statistical collection of data for their chemical composition, oxide dispersions were analysed to be 13Cr–57Nb–31O in the as-cast condition. Note that oxides are occasionally accompanied by large porosity, as indicated in Fig. 3(a), also compare Fig. 3(a) with Fig. 3(d).

The results of the electron probe analyses of the Cr–2Nb–1Zr alloy annealed at 1473 K for 100 h were similar to those observed in the Cr–3Nb alloy. In the as-cast condition of this alloy, the Cr-rich dendritic phase contained 1.8 at.% Nb and 0.07 at.% Zr (Table 1), while the eutectic Cr_2X contained 13.9 at.% Nb and 10.8 at.% Zr. By annealing at 1473 K for 100 h, the Nb and Zr concentrations in the Cr-rich matrix phase reduced to 0.9 at.% Nb, and 0.02 at.% Zr, respectively. Correspondingly, the Nb concentration in the Cr_2X

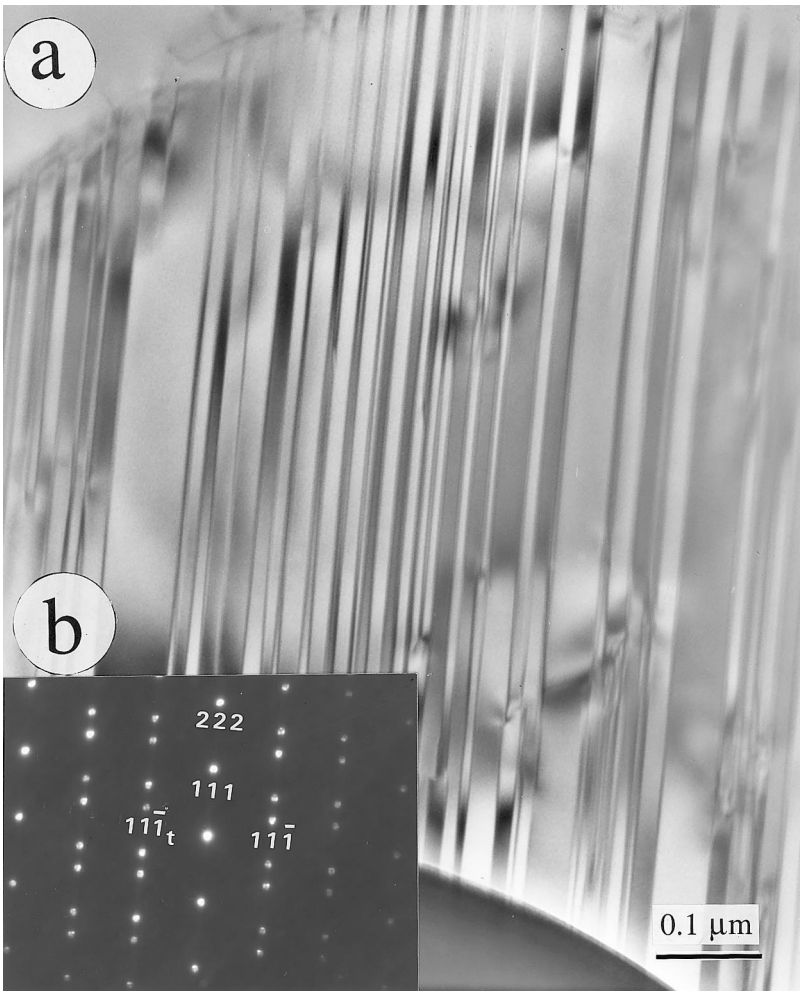

Fig. 5. (a) TEM bright field image of the eutectic Cr_2Nb phase in the as-cast Cr–3Nb alloy, and (b) the associated SAD pattern.

increased to 20.6 at.% Nb, but the Zr concentration reduced to 8.1 at.% Zr. The partitioning ratio of Zr in the Cr_2X phase versus the matrix Cr solid solution phase is 150:1 in the as-cast condition and 400:1 in the annealed condition. Thus, Zr strongly partitions to Cr_2X precipitates. A number of oxide dispersions were observed in the Nb–Cr–Zr ternary alloys as well. However, quantitative WDS analysis showed that the oxides contain Zr as the major constituent element and thus they are different from the composition of the oxides observed in the binary Cr–Nb alloy.

Microstructures of some of the alloys were examined in the TEM in the as-cast condition as well as in the annealed condition (1473 K for 100 h). Fig. 4 shows a TEM bright field image of the Cr–3Nb alloy in the as-cast condition. Cr_2Nb eutectic microconstituents are clearly visible and they are distributed in the form of a network, as previously observed by OM. The first point to be noted in this TEM image is that Cr_2Nb Laves phase particles exhibit micro-twins, as shown in a highly magnified TEM bright field image (Fig. 5a). Selected area diffraction (SAD) analysis indicates that the eutectic Cr_2Nb Laves phase has the cubic C15 structure and twinning is of the $\{111\}<112>$ type (see Fig. 5b). In the matrix (Cr-rich solid solution phase) adjacent to the Cr/Cr_2Nb eutectic region, a high density of dislocations is occasionally observed in an isolated form or in a piled-up form.

After annealing at 1473 K for 100 h, the Cr–3Nb alloy was found to have extensive solid-state precipitation of Cr_2Nb within the matrix Cr-rich phase, as shown in Fig. 6. In this photo, a narrow PFZ adjacent to a grain boundary is apparent. At the grain boundary, Cr_2Nb precipitates are also observed. The Cr_2Nb precipitates that result in the matrix from the annealing step are rod-shaped, with dislocations possibly originating at their interfaces. These Cr_2Nb precipitates were also determined to have the C15 structure, and they were also twinned with a twinning relationship of the type $\{111\}<112>$.

Fig. 7(a) shows a TEM bright field image of the Cr–Nb–Zr alloy in the as-cast condition. The Cr_2X phase was found to delineate the interdendritic regions, forming a continuous, film-like layer, although such

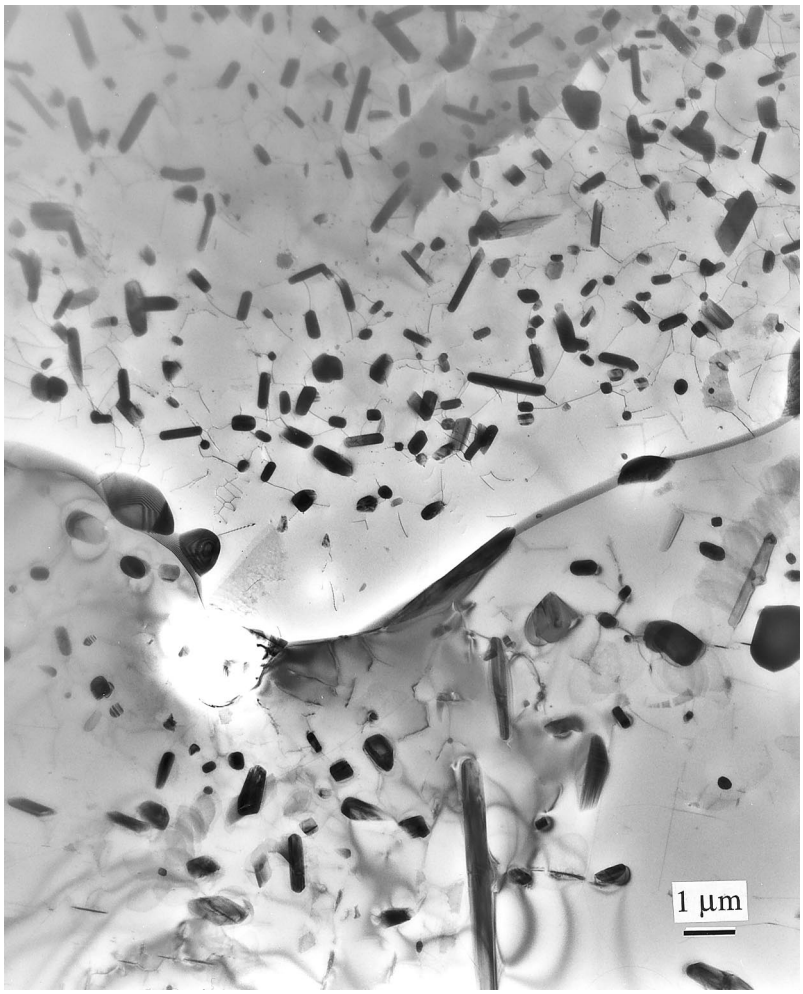

Fig. 6. TEM bright field image of the Cr–3Nb alloy annealed at 1473 K for 100 h.

details were not revealed by metallography (Fig. 2e). The Cr_2X phase was extensively faulted, as shown in Fig. 7(b). Dislocations were observed in the matrix adjacent to the eutectic Cr/Cr_2X region which may have been generated because of thermal mismatch stresses between these two phases.

Annealing at 1473 K for 100 h in the Cr–2Nb–1Zr alloy resulted in a microstructural change similar to that observed in the Cr–3Nb alloy; extensive amount of additional solid-state Cr_2X precipitation took place in the Cr-rich matrix, as shown in Fig. 8(a). An apparent PFZ adjacent to the eutectic Cr/Cr_2X region is found, and the precipitates within the matrix exhibit a rod morphology. The rod-shape precipitates are mostly accompanied by dislocations in the matrix originating from the Cr/Cr_2X precipitate interface. Fig. 8(b) shows a TEM bright field image of the eutectic Cr_2X phase in the Cr–2Nb–1Zr alloy annealed at 1473 K for 100 h. An extensively faulted structure is observed even after prolonged annealing at 1473 K. Selected area diffraction confirmed the phase to have the cubic C15 structure.

3.2. Mechanical properties

art summarises the results of room temperature Vickers hardness tests. As can be seen in Table 2, and also in Fig. 9(a), the overall hardness in the as-cast condition decreases in the order of, Cr–6Nb > Cr–5Nb–1Zr > Cr–3Nb > Cr–2Nb–1Zr ≫ Cr–1Zr > Cr–0.3Zr. It is noted that the two Zr-containing binary alloys showed substantially low hardness values in comparison to the Nb containing alloys. It appears that the observed hardness in the as-cast condition is primarily dependent on the volume fraction of the Cr_2X phase. The alloys with a large volume fraction of Cr_2X precipitates (e.g. the Cr–6Nb and Cr–5Nb–1Zr alloys), showed higher hardness than the alloys with a small volume fraction of Cr_2X precipitates (e.g. Cr–1Zr and Cr–0.3Zr alloys). With the increase in annealing time at 1473 K, the overall hardness of the Nb containing alloys showed an initial decrease, followed by an increase, with a small maximum located at ≈24 h annealing Fig. 9(a). On the other hand, the hardness obtained from indentations restricted to within the

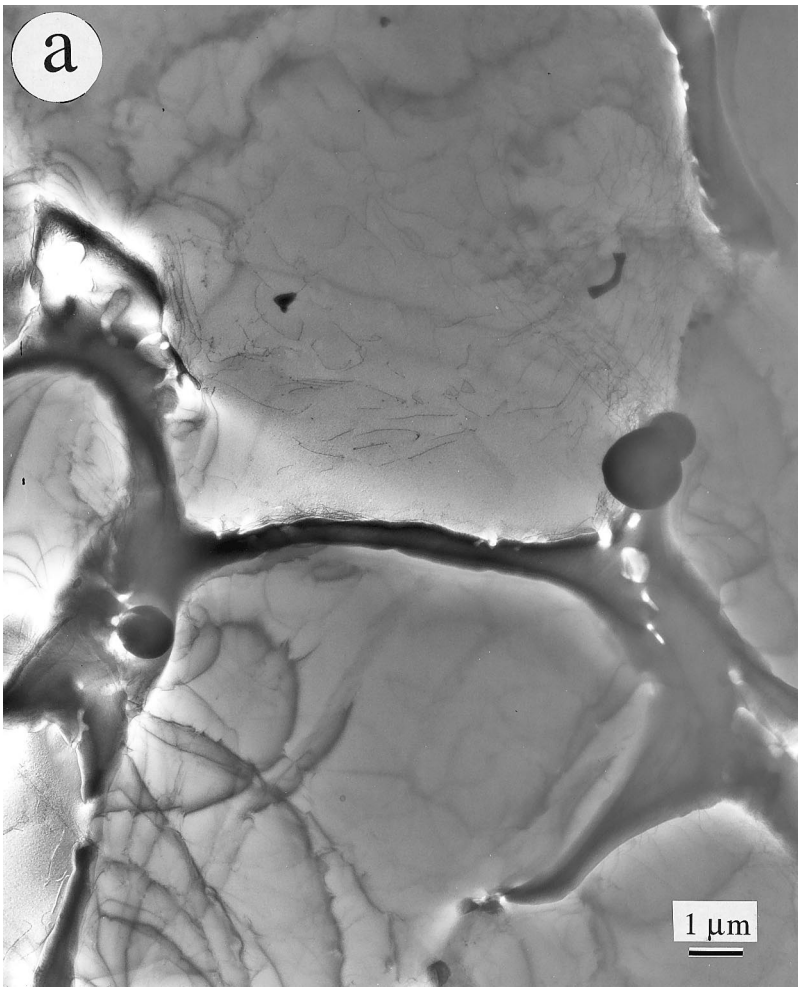

Fig. 7. TEM bright field images of (a) the as-cast Cr–2Nb–1Zr alloy, and (b) the eutectic Cr_2X phase in the as-cast Cr–2Nb–1Zr alloy.

Cr-rich matrix regions is higher in Cr–6Nb and Cr–5Nb–1Zr alloys than in Cr–3Nb alloy, as shown in Fig. 9(b). Also, the latter alloy was insensitive to annealing time. The change of the hardness with annealing time (overall alloy hardness or the hardness of the Cr-rich matrix region) may be related to the competition between solid-state precipitation of Cr_2X during annealing and solid solution hardening loss in the Cr-rich solid solution. It is worth reiterating that the 1473 K heat treatment has been referred to as an annealing step but the microstructural response is one more characteristic of ageing where supersaturation is relieved in the Cr-rich matrix phase by the solid state precipitation of the Cr_2X phase. On the other hand, the overall hardness of the two Zr-containing binary alloys decreased only slightly with annealing time. This change appears to be simply due to coarsening of the eutectic Cr_2Zr phase. Table 2 also lists hardness data determined by an indentation load of 5 kg. These values are generally identical to those determined by small indentation loads. No cracks associated with indentation were observed for all the alloys, in both the as-cast and annealed conditions.

Table 3 summarises the results of room temperature bending tests for all the alloys. Measurements were carried out in the as-cast condition and in the two annealed conditions (i.e. for 20 and 100 h at 1473 K). The load versus displacement curves typically displayed a linear behaviour with no appreciable plastic deformation prior to fracture. The observed bend strength could not directly be correlated with the hardness results. In the as-cast condition, the highest bend strength was observed in the Cr–0.3Zr alloy with the lowest volume fraction of Cr_2X precipitates and a low solubility of Zr element in the Cr-rich solid solution. In the binary Cr–Nb alloys as well as in the binary Cr–Zr alloys, high bend strengths were observed in the alloy with a low volume fraction of the eutectic Cr_2X phase (i.e. with low contents of Nb, and Zr, respectively). On the other hand, the two Cr–Nb–Zr ternary alloys exhibited significantly low bend strength as compared with other binary alloys. The bend strength appears not to be strongly affected by annealing at 1473 K for all the alloys.

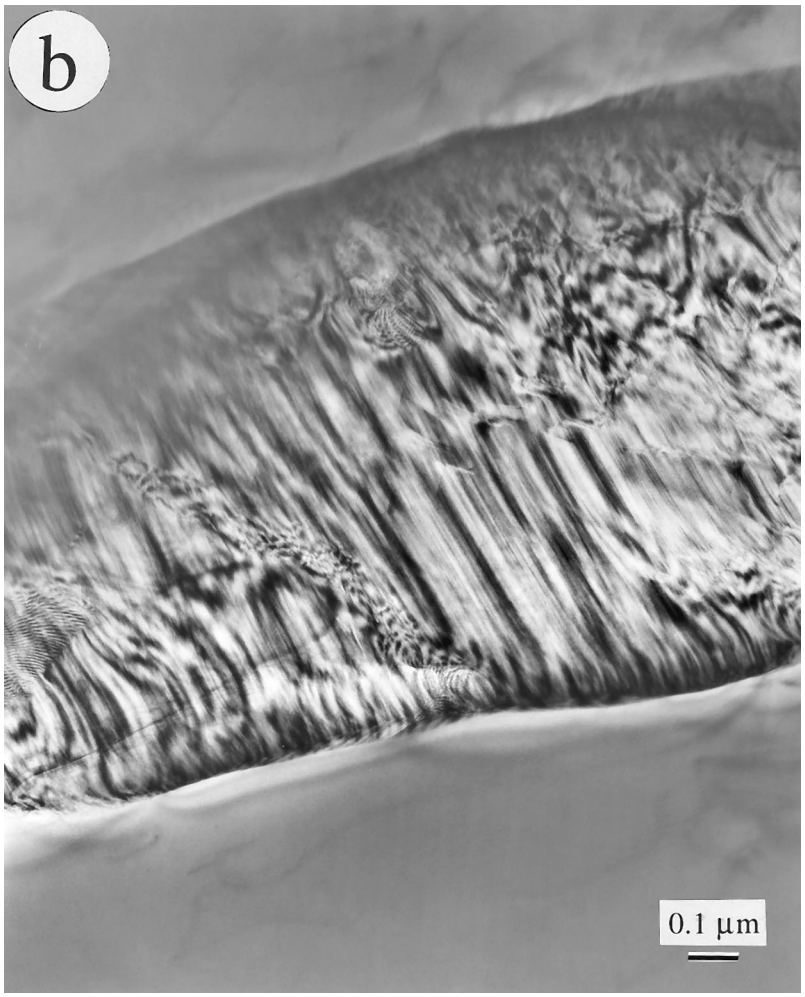

Fig. 7. (*Continued*)

The fracture surface of bend samples in the as-cast condition was examined by SEM. Figs. 10 and 11 show typical failure modes for the Cr–3Nb alloy, and the Cr–2Nb–1Zr alloy, respectively. The former alloy with a relatively high bend strength shows cleavage fracture mode with river-like patterns in almost the entire fractured area, while the latter alloy with a low bend strength showed a mixed fracture mode of cleavage fracture and interdendritic fracture. In the interdendritic fracture area, the cell size identified by SEM (see Fig. 11c), was actually identical to the cell size observed by OM (see Fig. 2e and f). Thus, it appears that the interdendritic fracture mode arising either due to shrinkage porosity or a continuous brittle interdendritic second phase film (or both), has the effect of reducing the room temperature crack resistance of the Zr containing alloys. Casting porosity (sometimes accompanied with oxide dispersions) was often observed in all the alloys. It is likely that these defects adversely affect the bend strength and the crack resistance of the alloys.

4. Discussion

It was confirmed from the present study that the maximum solubility limit of Nb in the Cr-rich phase is quite different from that of Zr, as reported previously [1,5]. This difference can be understood based on Hume-Rothery's rule. The atomic size effect may be a controlling factor because the electron concentration (e/a) factor is identical for the two solutes in this case. The (Goldschmidt) atomic diameters of the atoms, Cr, Nb and Zr are 0.257, 0.295, and 0.321 nm, respectively. Consequently, misfit values between solvent (i.e. Cr) and solute are calculated to be 14.8 and 24.9% for Nb, and Zr solutes, respectively. These values clearly predict that Nb is more soluble in the Cr-rich phase than Zr, consistent with the observed result.

The eutectic Cr/Cr_2X structures and the related coring effect in the Cr-rich phase were observed in all the alloys prepared in this study even though the solute concentrations in some of the alloys were below their equilibrium maximum solubility limits. This result is due to the cooling rate associated with drop casting.

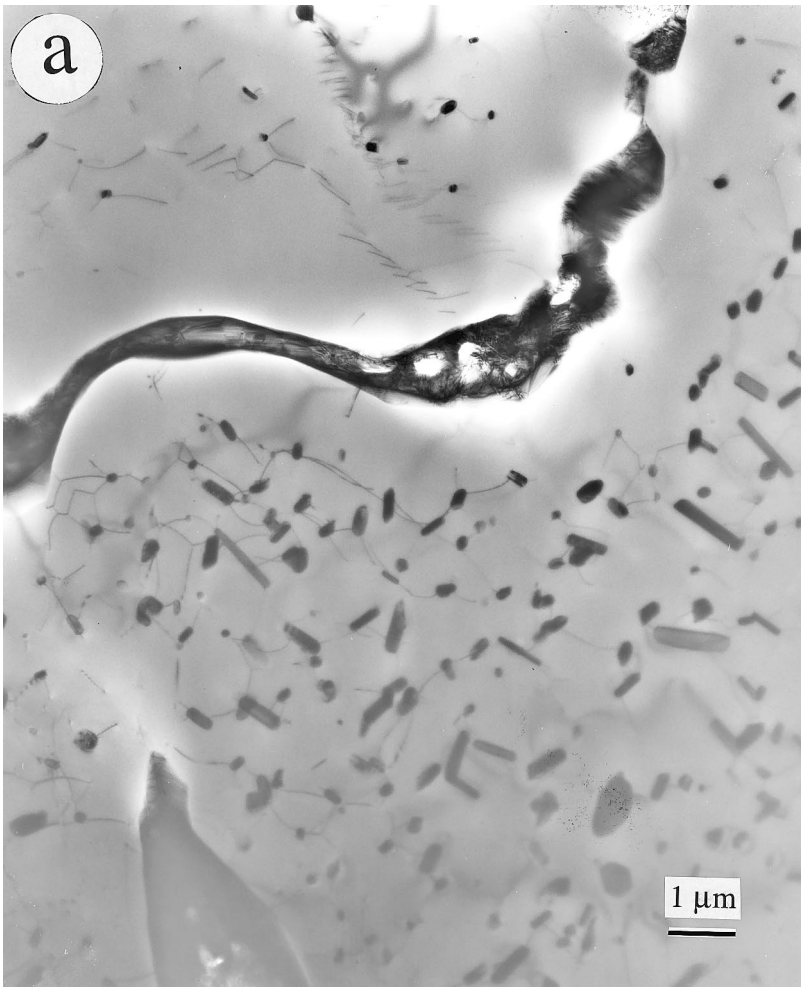

Fig. 8. TEM bright field images of (a) the Cr–2Nb–1Zr alloy annealed at 1473 K for 100 h, and (b) the eutectic Cr_2X phase in the annealed alloy.

For non-equilibrium cooling, if we assume both diffusion in the solid and convective and diffusive mixing in the liquid to be negligible, and also approximate the liquidus and solidus to be straight lines, then the partition coefficient, k is defined as c_s/c_L where c_s and c_L are the concentrations of solute in the solid, and liquid, respectively. In the case of the Cr–Nb alloy, $k = 5.6/18.5 = 0.3$ can be estimated from Fig. 1(a). The first solid to form (at the centre of dendrites) has a composition of kc_0 (where $c_0 = 3$ at.% Nb), i.e. 0.91 at.% Nb. This value may be consistent with the concentrations ($1.1 \sim 1.9$ at.% Nb) of the Cr phases in the Cr–3Nb alloy shown in Table 1 (note that the values analysed by WDS are overcounted because an electron probe diameter is large and thereby takes signal from the outer region). The spatial distribution of solid composition outwards from the centre of a dendrite is given by the Scheil equation, $c_s = kc_0(1 - f_s)^{k-1}$ where c is the composition of the Cr solid solution and f_s is the fraction solidified [17]. Thus, the Nb concentration of the Cr solid solution increases with increasing the volume fraction of the solid, i.e. with growing the dendrite. When $f_s = 0.93$, compositions of solid and liquid at the solid–liquid interface are estimated to become ~ 5.6 at.% Nb, and ~ 18.5 at.%, Nb, respectively, and the liquid with a volume fraction of $f_L = 0.07$ forms a non-equilibrium eutectic structure in the Cr–3Nb alloy. Thus, if we assume that at 1473 K (homogenisation temperature) the Nb solubility is ~ 1.5 at.% (see Fig. 1a), then regions in the dendrite containing < 1.5 at.% Nb will not show substantial precipitation in the solid state. On the other hand, similar calculation for the Cr–6 at.% Nb alloy predicts that the volume fraction of non-equilibrium eutectic microstructure is $f_L = 0.20$, which is higher than that of the Cr–3 at.% Nb alloy, and also that the Nb concentration at the centre of dendrites has a composition of $kc_0 = 1.8$ at.% Nb, resulting in complete precipitation by homogenisation. Thus, the observed microstructures are consistent with the estimation based on the Scheil equation [17]. In the Cr–Zr binary alloys, solid-state precipitation of Cr_2Zr particles was not observed even in the annealed materi-

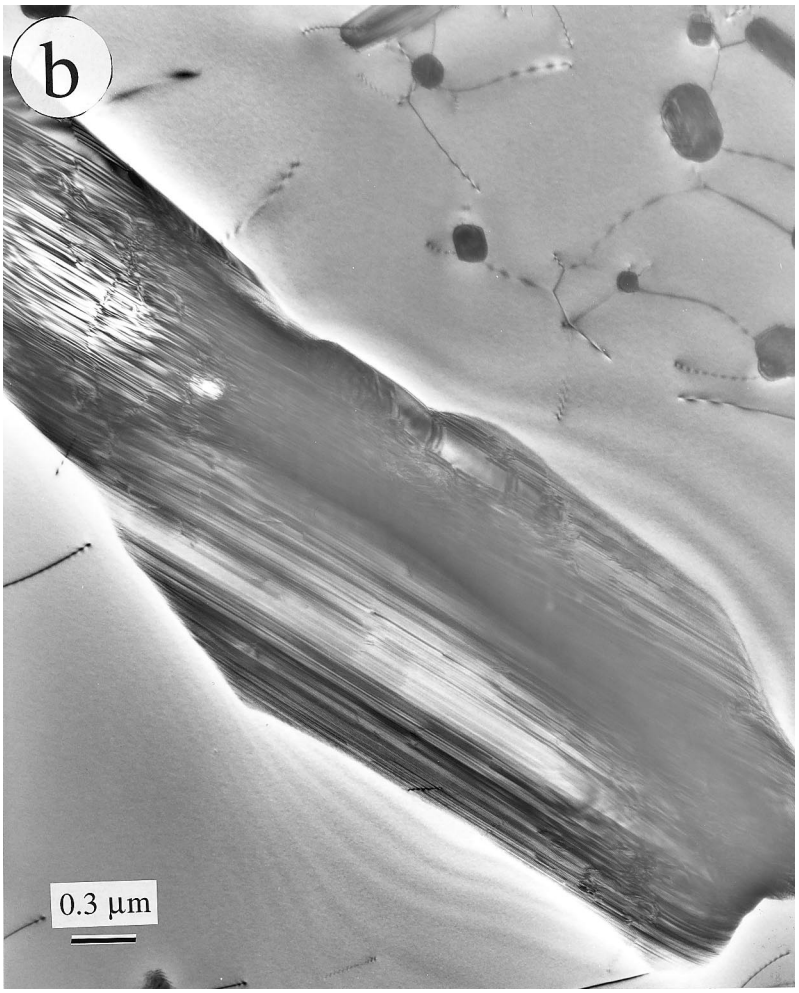

Fig. 8. (*Continued*)

als, at least at an optical microscopic level. This is most probably due to the negligible solubility change with temperature although the slow kinetics of solid-state precipitation during the 1473 K anneal (i.e. a slow diffusion rate of Zr in the Cr matrix, and/or slow nucleation and growth rates of precipitation) cannot be discounted.

It was found that the eutectic Cr_2X Laves phase in the binary Cr–Nb alloy in the as-cast condition consists of the C15 structure. The binary Cr–Nb phase diagram (see Fig. 1 a) indicates that the C14 structure is stable at the eutectic temperature and that it transforms to the C15 structure at a temperature below the eutectic temperature. It is evident from the present study that the C14 structure was not retained with the cooling rate associated with drop casting technique used in this study. The transformation from the C14 to C15 structures, in principle, can be accomplished via the synchroShockley-partial dislocation mechanism [18,19], and the C15 structure can also be twinned by a similar mechanism. Specifically, it has been proposed [19], that twinning of the type $\{111\}<112>$ occurs in the C15 structure by the motion of synchroShockley dislocations through each triple layer of the C15 structure (a unit four-layer stack composed of a triple layer plus a single layer is used to describe stacking sequences in Laves phases); if the same synchroShockley operates on successive planes, macroscopic shear results. Alternately, a set of three synchroShockleys with zero net Burgers vector can produce the same result with no macroscopic shear. On the other hand, the Cr_2Nb resulting from solid-state precipitation in the Cr-rich matrix during annealing (at 1473 K for 100 h) also consisted of the twinned C15 structure. The exact reason for the presence of twins (growth versus deformation twins) in these precipitates is not known and remains to be investigated.

The structure of the interdendritic film-like phase in the ternary Cr–2Nb–1Zr alloy in the annealed condition was confirmed to be C15; WDS showed that most of the Zr partitions to this phase, and the Zr level in the matrix in the as-cast condition as well as after annealing is low. There is a decrease in the Zr level in the matrix by annealing. Thus, Zr content is probably

Table 2
Vickers hardness[a] of the overall area and of the Cr-rich phase

Alloy number	Phases	As-cast	Heat treatment at 1473 K		
			5 h	20 h	100 h
Cr–6Nb	Overall	411(418)	367	366	254(298)
	Cr phase	368	313	289	276
Cr–3Nb	Overall	314(299)	266	281	252(233)
	Cr phase	242	242	244	240
Cr–1Zr	Overall	144(135)	143	137	132(125)
	Cr phase	–	–	–	–
Cr–0.3Zr	Overall	136(127)	116	120	114(108)
	Cr phase	–	–	–	–
Cr–5Nb–1Zr	Overall	343(408)	310	342	288(303)
	Cr phase	318	306	332	280
Cr–2Nb–1Zr	Overall	300(297)	269	267	241(223)
	Cr phase	–	–	–	–

[a] Vickers hardness in overall area was measured using an indentation load of 500 g or 5 kg (shown in parentheses), while Vickers hardness in Cr-rich phase was measured using an indentation load of 50 g.

initially low in the Cr_2X phase that results from solid state precipitation within the matrix during annealing. Long-term annealing may result in Zr transfer from the interdendritic phase to these second generation precipitates in an attempt to attain equilibrium. Further experiments are required to verify this hypothesis.

The existence of oxides indicates that the alloys prepared in this study are contaminated by gaseous element such as oxygen. The source of the contamination is not known but could be from the raw materials and/or the arc-melting process. Pure Cr charge material was analysed to contain as much as 2000 wtppm O. Whereas Nb-based oxides were identified in the Cr–Nb alloys, Zr-based oxides were present in the Cr–Nb–Zr ternary alloys. The reason for the formation of such oxides is not clear at present because their structures and compositions were not carefully determined in this study. The room temperature formation energies of some oxides which could be formed in the alloys are available: $\Delta H Cr_2O_3 = -1130$ kJ mol^{-1}; $\Delta H Nb_2O_5 =$

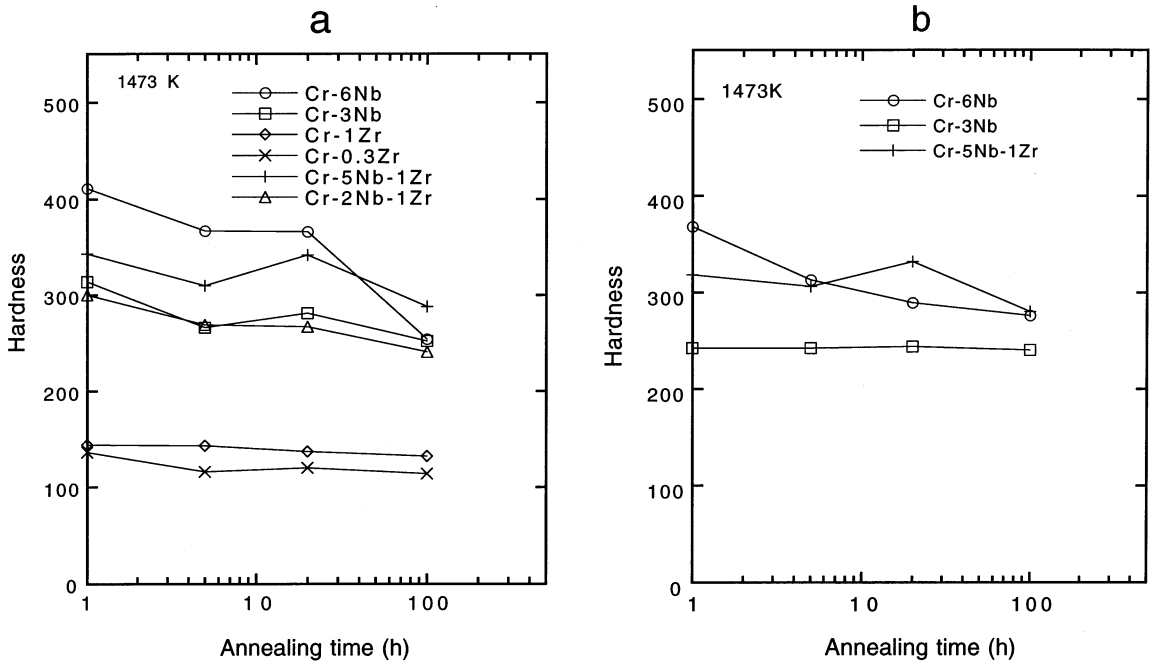

Fig. 9. Changes of Vickers hardness with annealing time at 1473 K. In (a) the overall Vickers hardness measured using a 500 g load is shown, while in (b) Vickers hardness of the primary Cr-rich solid solution phase measured using a 50 g load is shown. Note that the data for the as-cast condition are plotted on the y-axis.

-1904 kJ mol^{-1}; ΔHNbO $= 412$ kJ mol^{-1}; ΔHNbO$_2 = -797$ kJ mol^{-1}; and ΔHZr$_2$O $= -1100$ kJ mol^{-1}. However, the preference of oxides identified in this study cannot be explained based on such thermodynamic data.

The Cr–Nb alloys were harder than the Cr–Zr alloys, and also the alloys with higher concentrations of Nb and Zr were harder than those with lower concentrations, as shown in Fig. 9, and Table 2. This result indicates that the hardness of the alloys primarily depends on the volume fraction of the hard Cr_2X phase. The hardness also depends on Cr_2X particle size. For example, it is possible to attribute the high hardness of the Nb–6Cr alloy to the combined effect of a supersaturated solid solution matrix and fine precipitation of Cr_2Nb in the Cr-rich solid solution. When these particles coarsen (following extended annealing), the Nb–6Cr alloy is not harder than the Nb–5Nb–1Zr alloy (see Fig. 9a). Therefore, there may be an optimum annealing condition resulting in the maximum strength (or hardness) or the crack resistance, depending on the alloy system and composition.

The room temperature bend strength and fracture behaviour may be well related to the morphology and distribution of Cr_2X precipitates. The Cr–Nb–Zr ternary alloys exhibited substantially low bend strength (Table 3). Such low fracture strength is related to the decohesion of interdendritic boundaries delineated by Cr_2X precipitates, as clearly identified by TEM (Fig. 7a) and SEM (Fig. 11) observations. This result reveals that the strength of the matrix–Laves phase interface is an important factor for low temperature fracture toughness. More work is necessary to clarify the effect of ternary element on morphology and interface property of the Laves precipitates. Also, porosity and oxides play a role in fracture behaviour but it may not be a major one, as suggested from the data in Table 3.

Table 3
Bending strength of the alloys used in this study

Alloy	Heat treatment	Fracture strength (N mm^{-2})
Cr–6Nb	As-cast	183
	1473 K/20 h	211
	1473 K/100 h	127
Cr–3Nb	As-cast	372
	1473 K/20 h	287
	1473 K/100 h	303
Cr–1Zr	As-cast	181
	1473 K/20 h	196
	1473 K/100 h	277
Cr–0.3Zr	As-cast	494
	1473 K/20 h	364
	1473 K/100 h	417
Cr–5Nb–1Zr	As-cast	81[a]
	1473 K/20 h	195[a]
	1473 K/100 h	20[a]
Cr–2Nb–1Zr	As-cast	84[a]
	1473 K/20 h	82[a]
	1473 K/100 h	69[a]

[a] The specimen had visible large pores prior to the test.

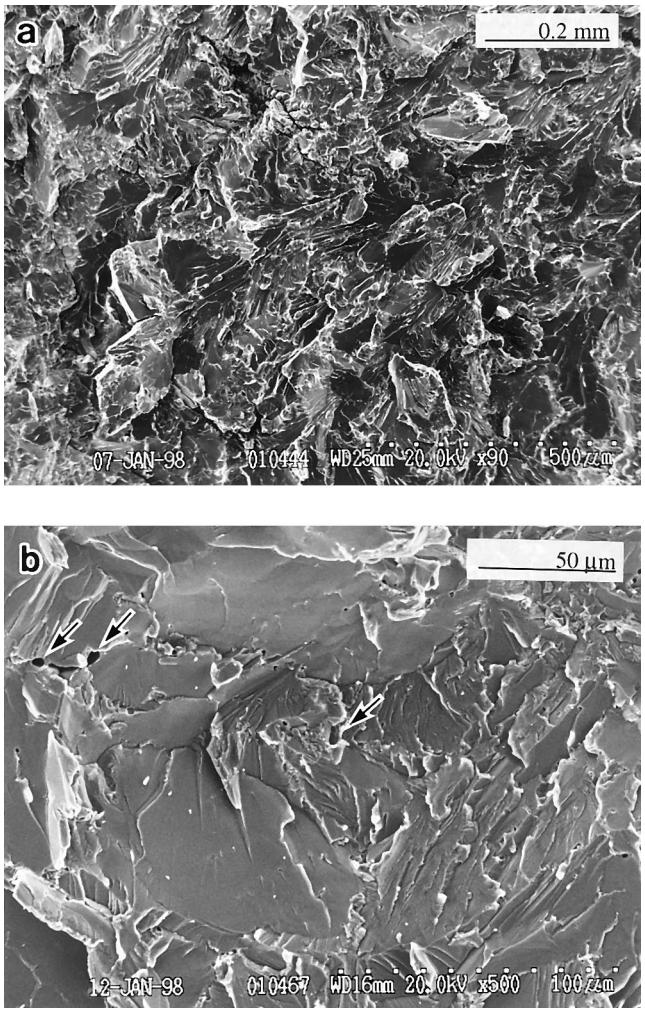

Fig. 10. SEM images of the bend fracture surface of the as-cast Cr–3Nb alloy. Note that porosity is denoted by arrows.

5. Conclusions

Two-phase Cr–Nb, Cr–Zr and Cr–Nb–Zr alloys with alloying levels in each instance below or close to maximum solubility in Cr, were studied in terms of microstructure and mechanical properties, and the following results were obtained.

1. The microstructures of the as-cast alloys show a primary Cr-rich solid solution dendrites surrounded by an interdendritic Cr/Cr_2X eutectic structure. Upon annealing at 1473 K, solid state precipitation of Cr_2X Laves phase takes place within the Cr-rich solid solution matrix of the Cr–Nb and Cr–Nb–Zr alloys but not in the binary Cr–Zr alloys. This

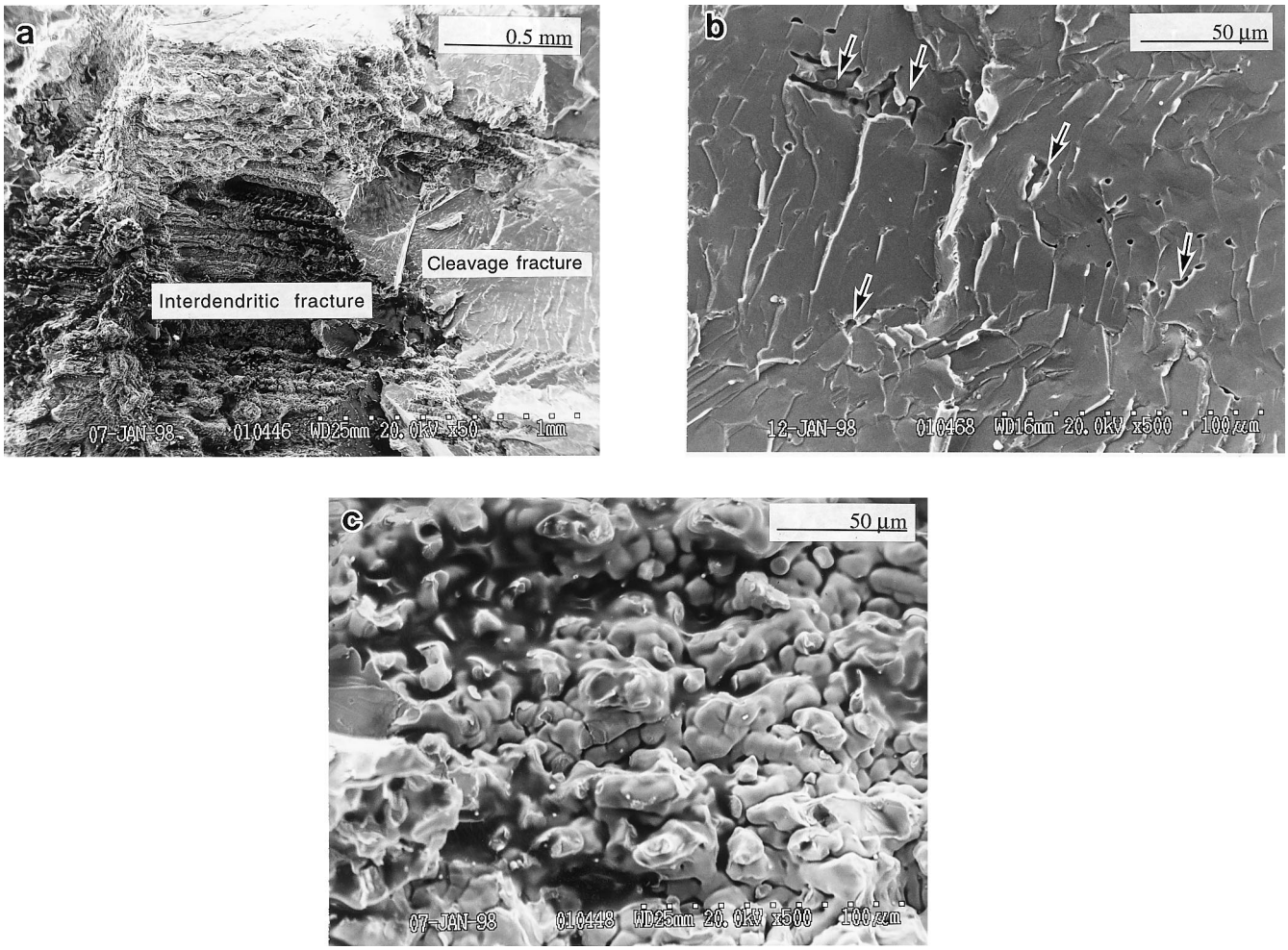

Fig. 11. SEM images of the as-cast Cr–2Nb–1Zr alloy. Note that the cleavage area is shown at a high magnification in (b), while the interdendritic fracture area is shown at a high magnification in (c). Also, pores (occasionally accompanied with dispersions) are denoted by arrows in (b).

discrepancy is attributed to the difference in the solubility change with temperature.

2. Cr_2Nb Laves phase resulting from the eutectic decomposition as well as the solid-state precipitation consists of the C15 structure accompanied by $\{111\}<112>$ twins. Zr strongly partitions to the Cr_2Nb Laves phase and occupies the Nb sublattice sites. The addition of Zr to the Cr–Nb results in more faulted structure, and the faulted structure is retained even in the annealed material.
3. Oxides were present in these alloys. The oxides in the Cr–Nb alloys contained Nb as the major constituent, while the oxides in the Cr–Nb–Zr alloys contained Zr as the major constituent.
4. Vickers hardness primarily depends upon the volume fraction of the Cr_2X Laves phase. The largest and lowest hardness values were observed in the 6 at.% Nb-containing alloy, and in the 0.3 at.% Zr-containing alloy, respectively. An age-hardening behaviour was observed in the Cr–Nb and Cr–Nb–Zr alloys upon annealing at 1473 K.
5. The highest bend strength was obtained in the Cr–0.3 Zr alloy with the lowest volume fraction of the Cr_2X Laves precipitates. The room temperature bend strength is strongly affected by the formation of interdendritic Cr_2X precipitates, along with casting porosity and oxides in the alloys.

Acknowledgements

The authors are grateful to J.H. Zhu for preparation of alloys used in this study, J.L. Wright for his technical assistance, and L.R. Walker for electron microprobe analysis. This research was sponsored by the Division of Materials Sciences, US Department of Energy, under contract DE-ACO5-960R22464 with Lockheed Martin Energy Research Corporation.

References

[1] T.B. Massalski, J.L. Murray, L.H. Bennett, H. Baker (Eds.), Binary Alloy Phase Diagram. American Society for Metals, Metals Park, OH, 1986.

[2] M. Takeyama, C.T. Liu, Mater. Sci. Eng. A132 (1991) 62.

[3] D.L. Anton, D.M. Shah, High Temperature Ordered Intermetallic Alloys IV, in: L.A. Johnson et al., (Eds.), MRS Symp. Publication, vol. 213, p.733, (1991).

[4] D.M. Shah, D.L. Anton, High Temperature Ordered Intermetallic Alloys IV, in: L.A. Johnson et al., (Eds.), MRS Symp. Publication, vol. 213, p.63, (1991).

[5] D.J. Thoma, J.H. Perepezko, Mater. Sci. Eng. A156 (1992) 97.

[6] D.L. Anton, D.M. Shah, High Temperature Ordered Intermetallic Alloys, V.I. Baker et al., (Eds.), MRS Symp. Publication, vol. 288, p.141, (1993)

[7] K.S. Kumar, C.T. Liu, Acta Mater. 45 (1997) 3671.

[8] C.T. Liu, P.F. Tortorelli, J.A. Horton, C.A. Carmichael, Mater. Sci. Eng. A214 (1996) 23.

[9] D. Davidson, Metall. Mater. Trans. A 28 (1997) 1297.

[10] K.S. Kumar, D.B. Miracle, Intermetallics 2 (1994) 257.

[11] B.P. Bewlay, J.A. Sutliff, M.R. Jackson, H.A. Lipsitt, Acta Metall. 42 (1994) 2869.

[12] R.G. Rowe, D.W. Skelly, M. Larsen, Scr. Metall. 31 (1994) 1487.

[13] L.A. Chen, S.M. Allen, J.D.L. Livingston, High Temperature Ordered Intermetallic Alloys V, I. Baker et al., (Eds.), MRS Symp. Publication, vol. 288, p.373, (1993).

[14] K.C. Chen, S.M. Allen, J.D. Livingston, J. Mater. Res. 12 (1997) 1472.

[15] R.L. Fleischer, R.J. Zabala, Met. Trans. A 21 (1990) 2149.

[16] K.S. Chan, D.L. Davidson, J. Mater. 48 (10) (1996) 62.

[17] E. Scheil, Metallforshung 2 (1947) 69.

[18] P. Pirouz, P.M. Hazzeldine, Scr. Met. Mater. 25 (1991) 1167.

[19] P.M. Hazzledine, in: M.H. Yoo, M. Wuttig (Eds.), Twinning in Advanced Materials, The Minerals, Metals and Materials Society, Warrendale, PA, 1994, p. 403.